

# Spontaneous pinch-off in rotating Hele-Shaw flows

R. Folch,<sup>1</sup> E. Alvarez-Lacalle,<sup>2</sup> J. Ortín,<sup>2</sup> and J. Casademunt<sup>2</sup>

<sup>1</sup>*Universiteit Leiden, Postbus 9506, 2300 RA Leiden, The Netherlands*

<sup>2</sup>*Departament ECM, Universitat de Barcelona, Av. Diagonal 647, E-08028, Barcelona, Spain*

The dynamics of the interface between two immiscible fluids in a rotating Hele-Shaw cell are studied experimentally, theoretically and by phase-field simulations of the H-S equations using standard boundary conditions. As the central, denser fluid is centrifuged, it forms fingering patterns with long, thin radial filaments ended by a droplet, alternating with incoming fingers of the outer, less dense fluid. Simulations show the length (width) of the filaments to grow (decay) roughly exponentially, and the incoming finger tips to asymptotically approach a finite radius for  $n$ -fold symmetric initial conditions; these thus tend to a stationary-shape “star-fish”, whose form is calculated. The filament width decays with a time constant which depends only on the viscosity contrast, whereas its length exhibits a completely universal growth rate; the latter is related to the run away of an isolated droplet, for which we give an exact solution. The exponential behavior is clear for high viscosity contrasts  $A$ , but important deviations are found for low  $A$ . Both experiments and simulations show systematic pinch-off of the droplets at the tips of the filaments for low and not for high  $A$ . A lubrication approximation is derived and successfully accounts for the filament thinning and the differences with  $A$ ; in particular, it explains why pure exponential thinning is not observed for low  $A$ , and it could clarify the presence or absence of finite-time pinch-off itself, since the agreement of experiments and simulations suggests that this phenomenon is contained in the Hele-Shaw equations. This agreement includes both high- and low- $A$  morphologies, and the growth rate of the filament length for high  $A$ ; for low  $A$ , the experimental time constant appears to be different from that predicted by standard Hele-Shaw boundary conditions and observed in simulations. An effective slip condition for the Poiseuille flow of inner liquid across the cell gap in the case of two liquids gives a possible explanation of this discrepancy.

PACS numbers: 47.55.Dz, 47.20.Ma, 47.11.+j, 68.03.Cd

## I. INTRODUCTION

Topological singularities such as interface pinch-off in fluid flows have been the object of intense study in the last decades [1, 2, 3, 4, 5, 6, 7, 8, 9, 10, 11, 12, 13, 14]. The pinch-off of a droplet from a volume of fluid embedded in another one is easy to observe in everyday life, and has fascinated both physicists and applied mathematicians. Because the interface between the two fluids shrinks to arbitrarily small scales at the point of detachment, a continuum, coarse-grained description must break down at some stage. The failure of the macroscopic description is reflected in the spontaneous generation of singular behavior. In the neighborhood of such singularities, the problem might become scale-free, giving rise to self-similar scaling behavior, for which some degree of universality is naturally expected [1]. Interestingly, hydrodynamics alone have been found sufficient to account for the occurrence of finite-time pinch-off in several cases. It is remarkable that the continuum, hydrodynamic description may correctly predict the occurrence of finite-time singularities out of a smooth initial condition, and properly describe them all the way to the very microscopic scales where atomic-scale forces take over. These forces then implement the interface breakup and reconnection. This is the case, for instance, of three-dimensional jets [2]. The pursuit of this idea in the specific context of rotating Hele-Shaw flows is the basic motivation of the present study.

Recently, macroscopic hydrodynamic equations have

also been used as a basic ingredient in the dynamics of nanojets [3, 4], or in very thin membranes, where the effects of Van der Waals forces must be taken into account [5, 6]. These are examples of nonlinear processes where the macroscopic dynamics coupled with molecular forces or thermal noise lead to pinch-off phenomena.

In the narrow gap between the two parallel glass plates of a Hele-Shaw cell, the scale where the effective two-dimensional “macroscopic” description fails is basically the thickness of the cell gap [7]. Although this cutoff is much larger (typically, of the order of the millimeter) than the microscopic cutoff of the hydrodynamic description of 3d jets, it still makes sense to investigate to what extent the 2d effective dynamics in a Hele-Shaw cell (playing the role of the “macroscopic” dynamics) lead to the spontaneous occurrence of finite-time singularities. The interface recombination will certainly introduce new physics (not contained in the ordinary Hele-Shaw equations) which could easily depend on details that may not be universal, such as wetting conditions, 3d structure of the meniscus, contact line motion, etc.; the precise time of the pinch-off may also depend on these details. However, the underlying idea is that the effective cutoff and the details of the actual 3d pinch-off can in principle be arbitrarily reduced, for instance changing the cell gap. So, ultimately, the relevant question is what the prediction of the effective 2d (Hele-Shaw) dynamics is: If the 2d dynamics lead themselves to finite-time pinch-off, this would certainly assure the existence of finite-time pinch-off in the real experiments, and would also define

an upper bound for the actual experimental pinch-off. If, on the contrary, no finite-time pinch-off is obtained for the Hele-Shaw dynamics, it will be relevant to study the evolution of a thin neck as predicted by the effective 2d dynamics, in order to elucidate, in each particular case, whether actual pinch-off would be expected invoking the additional 3d effects. In this context, the simulations performed within a phase-field scheme are particularly appropriate, because they incorporate a natural cutoff (the interface thickness) which controls the actual pinch-off and which, like the cell gap in Hele-Shaw flows, can be modified at will to postpone the pinch-off of a narrow fluid filament.

It is well known that the effective two-dimensional Hele-Shaw dynamics can lead *per se* to pinch-off. In fact, it was for this type of dynamics that finite-time pinch-off singularities in a hydrodynamic description were first found [8, 9]. As opposed to the 3d case of a cylindrical interface, a 2d fluid filament (two parallel interfaces) is stable to the Rayleigh criterion: The total interface length (at constant area) is larger for any perturbation around straight interfaces. However, surface tension alone has been shown to drive a configuration of two droplets of fluid connected by a neck to finite-time pinch-off in two-dimensional simulations, for certain initial conditions [10, 11]. A straight filament of fluid can also be made to pinch at infinite time (and sometimes also at finite time), with very specific boundary conditions [8, 9, 12, 13, 14]. However, two-dimensional pinch-off in unprepared situations emerging spontaneously in externally driven dynamics, such as in traditional viscous fingering experiments, has not been addressed. One of our main goals is to account for the *spontaneous* approach to pinch-off singularities often observed while a highly nonlinear pattern develops following a morphological instability, in particular for rotating Hele-Shaw flows. Pattern formation and pinch-off singularities can indeed be intimately related, as it will become apparent in the case studied here.

Another issue that it is worth addressing is the role of the viscosity contrast or Atwood ratio  $A \equiv (\mu_{\text{in}} - \mu_{\text{out}})/(\mu_{\text{in}} + \mu_{\text{out}})$  (where  $\mu_{\text{in}}$  and  $\mu_{\text{out}}$  are the viscosities of the inner and outer fluids respectively) in the pinch-off process. It is known that this parameter has a strong influence on the interface shape near pinching in three dimensions [6], but only recently has it been remarked that the most studied limit  $A \rightarrow 1$  might be a very special case also in three dimensions [15]. In effectively two dimensions, experiments performed in this limit, with air displacing a liquid in a channel geometry, show that the fingers formed due to the morphological instability compete until a single finger is left [16]; the neck of the transient and final finger(s) does not even pinch. In contrast, when a denser liquid is put on top of a less dense one of similar viscosity (typically  $A \sim 0-0.5$ ) in the same but tilted channel, fingers do not compete, but elongate to form thin filaments with a droplet at their tip [17], which can indeed pinch off [18]. One possible scenario

to explain this different tendency to pinch-off might consist in relating the absence of competition for low  $A$  with the formation of long filaments, which could then pinch by mechanisms not qualitatively different from those of previous studies [8, 9, 10, 11, 12, 13, 14].

We have performed experiments in a rotating Hele-Shaw cell, where a drop of the more dense fluid is placed at the center and the instability is driven by the centrifugal force. The idea is to favor the formation of long (radial) filaments by the use of a driving force which increases as the fingers become longer. The natural question to pose is then whether these long filaments will also pinch for high viscosity contrasts.

Long fingers are indeed formed and they stretch and narrow for any viscosity contrast  $A$ . However, for high values of  $A$  we only observe pinch-off sporadically, whereas we find it systematically for low ones. This rules out the above scenario. It rather suggests that the precise nonlinear dynamics close to pinch-off, and not only the overall morphology, is also dependent on the viscosity contrast  $A$ . This dependence could either be contained in the (2d) Hele-Shaw dynamics or, instead, enter through different wetting properties for air-oil (high  $A$ ) and oil-oil (low  $A$ ) interfaces when the width of the filaments becomes comparable to the cell gap in our experiments.

We have run phase-field simulations of the two-dimensional dynamics which lead to pinch-off singularities for low, but not high viscosity contrast. Although we can only track the first stages of the approach, the major dependence of the pinching dynamics on the viscosity contrast thus seems to be contained in the Hele-Shaw equations. In particular, our simulations indicate that finite-time pinch-off could be contained (at least) in low- $A$  Hele-Shaw dynamics for more general settings than those originally studied in Refs. [8, 9, 10, 11, 12, 13, 14]. Therefore, it is plausible that the effect of the cutoff (here, the cell gap), although entering the problem earlier than in usual three-dimensional cases, can still be regarded as an implementation of pinch-off and reconnection, not necessarily affecting significantly the approach to pinch-off, which is governed by the Hele-Shaw dynamics.

The rest of the paper is organized as follows: In Sec. II we present the experimental results, with an indication of scaling behavior. This is then explained in the following section by simple theoretical arguments valid asymptotically. In Sec. IV we test this basic picture by numerical simulations of the Hele-Shaw equations. These confirm theory and experiments to agree for high viscosity contrasts, whereas puzzles remain for low ones. One of these can be solved by rethinking the experimental time scale as done in Sec. V, while another requires a refinement of the theory which is performed in Sec. VI. The results are summarized and further discussed in Sec. VII.

## II. EXPERIMENTAL RESULTS

We have performed two sets of experiments in a rotating Hele-Shaw cell: one for high and one for low viscosity contrast. These two types of experiments were already performed for other purposes in [19] and [20]; we repeat them here to address the scaling behaviors and the presence of pinch-off as functions of viscosity contrast. Our cell consists of two horizontal glass plates, 7 or 10 mm thick and 390 mm in diameter, separated by different spacers of height  $b = 0.5, 0.7, 0.8, 1.0, 1.4$  mm. The cell is rotated around a vertical axis intersecting its center, with a controlled frequency  $\Omega$ , and the interface shape is recorded with a CCD camera.

In a first set of experiments, a silicone oil of viscosity  $\mu_{\text{in}} = 50\text{cp}$  and density  $\rho_{\text{in}} = 975 \pm 10\text{kg/m}^3$  at  $20^\circ\text{C}$  and air are used as inner and outer fluids, respectively, in a prewetted cell [21]. This yields  $A = 1$  and  $\Delta\rho = \rho_{\text{in}} - \rho_{\text{out}} \simeq 0.98\text{g/cm}^3$ , and an interfacial tension  $\sigma = 20.7\text{mN/m}$ . In a second set of experiments, we use another silicone oil ( $\mu_{\text{in}} = 530 \pm 50\text{cp}$ ,  $\rho_{\text{in}} = 975 \pm 10\text{kg/m}^3$ ) as inner, and a vaseline oil ( $\mu_{\text{out}} = 190 \pm 50\text{cp}$ ,  $\rho_{\text{out}} = 875 \pm 10\text{kg/m}^3$ ) as outer fluid. In this case  $A = 0.45 \pm 0.05$ ,  $\Delta\rho \simeq 0.10\text{g/cm}^3$ ,  $\sigma = 1.8 \pm 0.7\text{mN/m}$ . Mean values are given at  $20^\circ\text{C}$ , and the uncertainty in the viscosities (and their contrast  $A$ ) accounts for temperature variations.

Figures 1(a,b) and 1(c,d) show the typical patterns formed at two different stages, for high ( $A = 1$ ) and low ( $A \simeq 0.45$ ) viscosity contrast, respectively. Although the nonlinear dynamics depend significantly on the viscosity contrast, as we can see, let us focus for the moment on those features which are generic to any value of  $A$ : After some latency time, the linear instability leads to small undulations on the initial circle of radius  $R_0$ . These undulations grow into radial fingers of silicone oil. As they are further centrifuged, the fingers develop overhangs; their tips evolve into differentiated droplets, whereas the overhang regions themselves narrow and stretch to become thin filaments, which continue to stretch and narrow. In parallel with this, incoming fingers of less dense fluid advance towards the cell center. However, they do not develop thin filaments nor droplets, and they slow down as they approach the cell center.

The filament thinning and the dynamics of the incoming fingers are rather difficult to measure accurately and not very sharply defined experimentally. In contrast, the stretching of an individual filament, or, more precisely, the radial coordinate of the droplet at its tip,  $R$ , is more readily accessible. The squares ( $A = 1$ ) and the circles ( $A \simeq 0.45$ ) in Fig. 2 indicate this droplet position (even after pinch-off) in units of the radius  $R_0$  of the initial circle and in log scale, as a function of time  $t$  in units of the time scale

$$t^* = \frac{12(\mu_{\text{in}} + \mu_{\text{out}})}{b^2\Omega^2\Delta\rho}. \quad (1)$$

The open squares and circles indicate the evolution of the furthest droplet in Figs. 1(a,b) and 1(c,d) respectively.

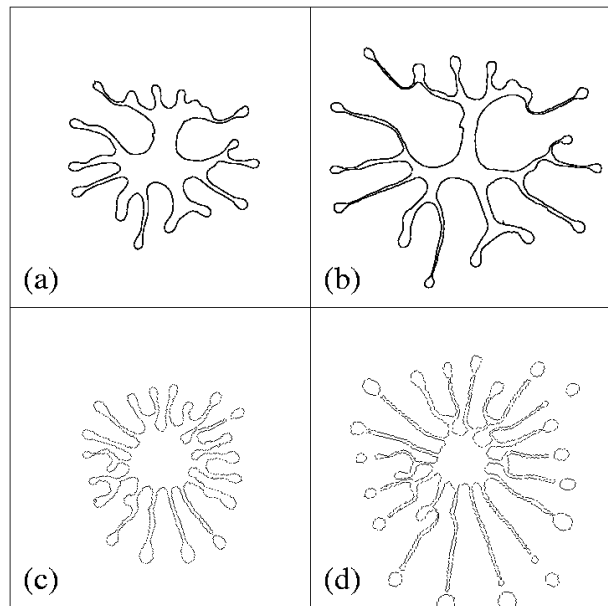


FIG. 1: Pattern evolution for  $A = 1$ ,  $b = 0.5\text{mm}$ ,  $\Omega = 120\text{rev/min}$  and  $R_0 = 50\text{ mm}$  (a,b), and  $A \simeq 0.45$ ,  $\Omega = 180\text{rev/min}$  and  $R_0 = 38\text{ mm}$  (c,d). Snapshots ( $3R_0 \times 3R_0$ ) 16.5s (a) and 22.5s (b), and 122s (c) and 158s (d) after beginning rotation.

As we can see, the growth tends to be roughly exponential, at least for  $R/R_0 > 2$ . (Note that  $R/R_0 < 2$  corresponds rather to relatively small fingers, rather than droplets at the tip of thin filaments). It seems reasonable to measure a growth rate—the slope of linear fits (solid lines) in Fig. 2; this yields  $m = 0.8\text{--}1.0$  with good linearity beyond  $R = 2R_0$  for  $A = 1$ , and  $m = 1.25\text{--}1.5$  for  $A \simeq 0.45$ .  $A \simeq 0.45$  curves tend to bend a bit more, but this eventual bending is uncorrelated with the droplet pinch-off: To check this, we have performed an experiment with an isolated, off-center circular droplet; it roughly keeps its circular shape and runs away at a very similar rate ( $m = 1.45$ , triangles).

The most striking difference between high ( $A = 1$ ) and low ( $A \simeq 0.45$ ) viscosity contrast is the systematic droplet pinch-off observed for low, but not high  $A$ . For the latter, filaments keep on growing and stretching, while reaching a width comparable to the cell gap, that is close to the natural cutoff. While we have not spanned the whole range of  $A$ , all previous evidence shows that the so-called low contrast behavior is qualitatively unchanged for most of the range of  $A$ , and only very close to  $A = 1$  significant differences are found. This has been recently discussed in Refs. [19, 22].

Another difference seems to be the growth rate of droplets (connected or not to filaments). The uncertainties in the viscosities are not sufficient to account for it: droplets seem to be centrifuged faster in dimensionless time for low than for high viscosity contrasts. Our discussion on this is postponed to Sec. V.

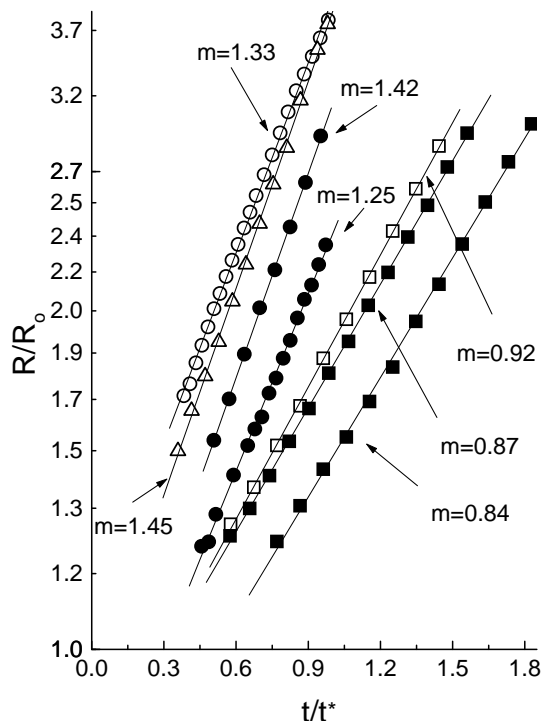


FIG. 2: Droplet kinetics: Evolution (as a function of scaled time) of the radial coordinate of (i) the center of mass of the drop at the tip of three different filaments for  $A \simeq 0.45$ , before and after pinch-off (circles); (ii) the center of mass of an isolated drop for  $A \simeq 0.45$  (triangles); (iii) the tip of three different filaments for  $A = 1$  (squares). Circles and triangle have been translated to earlier times for comparison. Open symbols correspond to the most excentric drops in Fig. 1;  $m$  are the slopes of linear fits.

### III. THEORETICAL SCENARIO

We try to link here by continuity arguments the filament thinning and stretching and the evolution of incoming fingers, and calculate the various growth and decay rates in a certain approximation. Because the dynamics of droplets at the tip of filaments should affect their stretching, we also construct an exact time-dependent solution for an off-center isolated droplet. Finally, we explore the existence of stationary-shape solutions as possible asymptotic attractors suggested by the slowing down of incoming fingers.

#### A. Scalings

Fluid incompressibility imposes fluid area conservation, which intuitively forces filaments to stretch and/or feed the droplet at their tip as they narrow, and fingers of less dense fluid to grow inwards as mass is transported outwards through the filaments. Area conservation hence seems an important feature of the dynamics. In partic-

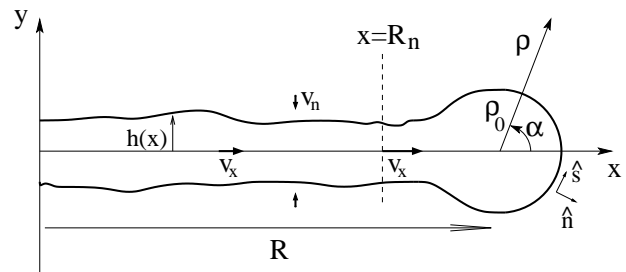


FIG. 3: Sketch of a filament of fluid with a droplet at its tip.

ular, “star-fish” patterns have been observed in an *ad hoc* geometrical model for the normal velocity of a front with *local* mass conservation on the interface (+ a constant flux) [23]. However, incompressibility also generally leads to *non-locality*, which will turn out to be crucial for low viscosity contrasts and for the presence of pinch-off singularities.

Let us first address the filament dynamics by means of a continuity equation in the overall direction of the filament  $x$ , which reflects the incompressibility of the inner fluid:

$$\partial_t h + \partial_x (h v_x) = 0, \quad (2)$$

where  $h(x, t)$  is the local  $y$  coordinate of either the upper or the lower interfaces, and  $v_x$  is the  $x$  component of the fluid velocity inside the filament (see Fig. 3).

Motivated by the experimental observations, we look for a scaling solution of the form

$$h(x, t) = L(t) h_0[xL(t)], \quad (3)$$

where  $L(t)$  is a dimensionless scaling factor. Substituting this ansatz into Eq. (2), we find

$$-\frac{\partial_t L}{L} = \frac{h_0 \partial_x v_x + v_x \partial_x h_0}{h_0 + x \partial_x h_0} = K, \quad (4)$$

where  $K$  is independent of  $x$ .

If  $v_x$  happens to be either (i) a constant along the filament or (ii) proportional to  $x$ ,  $v_x = Kx$ , a perfectly straight filament ( $h_0$  independent of  $x$ ) satisfies Eq. (4) and hence stays straight. Moreover, if and only if  $v_x = Kx$ , *any* function  $h_0(x)$  satisfies Eq. (4) and preserves its form. Interestingly, we will see that, for a straight filament, (i) corresponds to the standard channel geometry, and that our setup mostly falls in case (ii). In contrast, the radial case with injection, for example, cannot exhibit this type of self-similar solutions.

We find that, whenever the above scaling ansatz is valid, and further assuming  $K$  to be constant in time, then  $L = e^{-Kt}$ . The initial condition  $h_0(x)$  thus narrows exponentially

$$h = h_0 e^{-Kt} \quad (5)$$

and stretches

$$R_n = R_n(t=0) e^{Kt} \quad (6)$$

(where  $R_n = x \mid \partial_t h_0(x, t) = 0$ ) with a time constant set by the inner fluid velocity. Figure 3 schematically shows the in- and outgoing flow in this case. Eq. (6) is a statement that a reference point on the interface is advected with the filament as this is stretched. In particular, if applied to the neck of the filament just before the droplet as represented in Fig. 3, it would predict the total filament length to grow with the same time constant  $K$  with which its width decays. However, note that the outgoing flux of inner fluid at the neck can go into the droplet or contribute to the filament stretching. If some fraction of it actually goes into the droplet (as observed in the experiments), the scaling of the radial coordinate of the neck will be delayed with respect to the thinning rate  $K$ .

Finally, in order to relate this filament scaling with the incoming fingers, consider a reference circle of radius  $R_{\text{ref}}$  intersecting all filaments near their root, where they begin to look straight. The outwards flux of denser fluid through the circle and inside each filament is  $2h(t)v_{\hat{x}}(x = R_{\text{ref}})$ , and assuming again that  $v_{\hat{x}}(R_{\text{ref}})$  does not depend on time, we find it to scale as  $e^{-Kt}$ . In general, the area of denser fluid enclosed by this reference circle  $a$  should hence asymptotically decay with the same rate,

$$a = a(t \rightarrow \infty) + [a(t = 0) - a(t \rightarrow \infty)] e^{-Kt}. \quad (7)$$

A similar slowing down can then be expected for the radial position of the tips of identical incoming fingers.

## B. Exponential behavior and time constant

We now show that, *for a straight filament*,  $v_{\hat{x}}$  is linear in  $x$  as we anticipated, and we find the time constant  $K$ , which we have seen to set the time scale of the various exponential behaviors discussed so far. For that purpose, let us compute the tangential velocity jump across the interface.

The 2d velocity field  $u_i$  is proportional to the gradients of the pressure field  $p_i$  (Darcy's law), where the subscript  $i$  labels the inner ( $i = \text{in}$ ) and outer ( $i = \text{out}$ ) fluids. For a rotating cell [19]

$$\vec{u}_i = -\frac{b^2}{12\mu_i} \left( \vec{\nabla} p_i - \rho_i \Omega^2 r \hat{r} \right), \quad (8)$$

where  $r$  is distance to the rotation axis and  $\hat{r}$  is a unit radial vector pointing outwards. Using the standard boundary condition of Laplace law for the capillary pressure jump across the interface,  $p|_{\text{in}} - p|_{\text{out}} = \sigma\kappa$ , where the bar  $|$  stands for the limit value when approaching the interface from either side and  $\kappa$  is the interface curvature in the cell plane, we obtain

$$\hat{s} \cdot (\vec{u}|_{\text{out}} - \vec{u}|_{\text{in}}) = \frac{b^2}{6(\mu_{\text{in}} + \mu_{\text{out}})} (\sigma \partial_s \kappa - \Delta \rho \Omega^2 r \hat{r} \cdot \hat{s}) + A \hat{s} \cdot (\vec{u}|_{\text{in}} + \vec{u}|_{\text{out}}), \quad (9)$$

where  $s$  is a coordinate tangential to the interface and  $\hat{s}$  the unit vector in that direction.

In our sketch (Fig. 3), we identify  $v_{\hat{x}} \simeq \vec{u}|_{\text{in}} \cdot \hat{s}$ , which is a function of the local interface geometry and  $(1 - A)\vec{u}|_{\text{out}} \cdot \hat{s}$ , the solution of a non-local problem. To keep the problem local, we now assume that the outer fluid approaches the filament normal to it,  $\vec{u}|_{\text{out}} \perp \hat{s}$  (Note that this assumption is not necessary for  $A = 1$ ).

For a straight ( $\kappa = 0$ ) radial ( $\hat{x} \parallel \hat{r}$ ) filament, we obtain the anticipated  $v_{\hat{x}} = Kx$  and the time constant

$$K = \frac{b^2 \Delta \rho \Omega^2}{6(\mu_{\text{in}} + \mu_{\text{out}})(1 + A)} = \frac{2}{1 + A} \frac{1}{t^*} = \frac{b^2 \Delta \rho \Omega^2}{12\mu_{\text{in}}} \quad (10)$$

[case (ii) above]. One might wonder how a scale-free solution is possible without requiring the filament width to be much smaller than any other length scale, as it is legitimate to do close enough to pinch-off [1]. The answer is that the assumption of flatness has removed the capillary length (proportional to  $\sigma$ ) from the *local* problem; it still sets, together with the radius of the initial condition  $R_0$ , the size of e.g. the droplet at the tip of the filaments, but no external length scale can be felt when dropping the nonlocal term  $(1 - A)\vec{u}|_{\text{out}} \cdot \hat{s}$ . This allows for scaling solutions to exist well before pinch-off for  $A \equiv 1$ . It is this approach to pinch-off, rather than the pinch-off phenomenon itself, which will be further studied in this article.

For a tangential filament,  $K = 0$  and the filament is stationary [case (i) above], which is consistent with our observations for the tangential segments of some filaments. These segments are found where a tip split (for  $A = 0$ , see Fig. 1(c,d)) or at the point where an incoming finger was overcome and stopped by its neighbors (for  $A = 1$ , see Fig. 1(a,b)).

For the case of viscous fingering in a channel, the linear increase in the centrifugal force is replaced by a constant gravity (or equivalent injection). We can easily track this difference to yield a fluid velocity inside a filament parallel to the gravity or injection direction  $v_{\hat{x}}$  independent of  $x$ . The filament width will again be stationary [case (i) above]. We see by comparison that rotation not only ensures the formation of long filaments as we expected, but also brings the two interfaces close together.

For not completely straight filaments  $h(x)$ ,  $v_x \neq Kx$ . Therefore, strictly speaking, the scaling solution Eq. (3) does not hold for any  $h_0(x)$ , but only for a straight filament. It remains an approximate solution for slightly curved filaments (see Sec. VI), but it makes little sense for the droplets at the tip of the filaments. This raises the issue of dynamics of the droplet, which could potentially affect the filament stretching.

## C. Isolated droplet

The velocity found for the filament stretching has an elementary interpretation: In the overdamped limit associated to Darcy's law, all forces balance. The inner

fluid velocity  $v_x$  will hence be that which makes friction balance the other external forces, namely the centrifugal force and the force exerted by the outer fluid through its pressure gradients. The latter can be derived from another force balance, now in the outer fluid. There, the viscous forces vanish in the  $x$  direction with our assumption  $\vec{u}_{\text{out}} \perp \hat{s} \simeq \hat{x}$ , or even without this assumption for  $A = 1$ , since it corresponds to  $\mu_{\text{out}} = 0$ . Thanks to this, the other forces in the outer fluid (centrifugal and pressure gradients) balance in this direction. Thus, back in the inner fluid, friction,  $12\mu_{\text{in}}v_x/b^2$ , only needs to compensate for centrifugal forces,  $\Delta\rho\Omega^2x$ . This gives rise to the velocity found,  $v_x = Kx$  with  $K$  given by Eq. (10).

For a droplet (a closed interface), in contrast, the outer fluid needs to be moved in the  $x$  direction. The outer viscosity and velocity field enter the force balance, and  $v_{\hat{x}} \leq Kx$ , where  $v_{\hat{x}}$  is now the velocity of the center of mass of the droplet, and the equality holds only for  $A = 1$ . Except for  $A = 1$ , it is clear that the filament stretching will indeed be affected by this lower droplet velocity. Furthermore,  $v_{\hat{x}}$  will depend on the outer flow field, and hence on the droplet shape.

For a slightly off-center circular droplet,  $v_{\hat{x}}$  is known: Such a droplet corresponds to the mode 1 in a linear stability analysis of a circular, centered drop. Its growth rate is  $K' = 1/t^* = b^2\Delta\rho\Omega^2/[12(\mu_{\text{in}} + \mu_{\text{out}})]$  [19], where we readily see that it is the sum of viscosities, and not only the inner one, what counts.

We now compute the velocity for a circular droplet  $\partial_s\kappa = 0$  rigorously. Preserving the circular shape requires that  $\vec{u}_{\text{in}} = \dot{R}\hat{x}$  everywhere ( $R$  is distance from the rotation axis to the center of the droplet), so that the circle be just translated as a whole. We express the unit vectors tangential ( $\hat{s}$ ) and normal ( $\hat{n}$ ) to the interface and the radial vector  $\vec{r}$  connecting the rotation axis and a point on the interface in polar coordinates  $(\rho, \alpha)$  with respect to the center of the droplet (see Fig. 3), and compute  $\hat{s} \cdot \vec{u}_{\text{in}} = -\dot{R}\sin\alpha$  and  $\vec{r} \cdot \hat{s} = -R\sin\alpha$ . For  $A = 1$ , Eq. (9) reduces to a simple geometric relation between the two. Interestingly, like the filament scaling, this is verified either for a channel under injection or gravity ( $\dot{R}$  is then a constant) or for a rotating cell as presented here,  $\dot{R} = K'R$ , but not for a general driving force or geometry. We hence find that a circular off-center droplet is a time-dependent solution in a channel or rotating cell for  $A = 1$  as was previously found using conformal mapping techniques in [24].

For  $A < 1$ , the outer flow enters the problem. If a circular droplet is to remain a solution, it has to match the linear regime. At that stage, we will still have  $\dot{R} = K'R$ , regardless of the viscosity contrast. Substituting this into Eq. (9), we find  $\hat{s} \cdot \vec{u}_{\text{out}} = -\hat{s} \cdot \vec{u}_{\text{in}} = \dot{R}\sin\alpha$ . Continuity of normal velocities across the interface gives us  $\hat{n} \cdot \vec{u}_{\text{out}} = \dot{R}\cos\alpha$ , and we thus find the outer velocity on the interface to be  $\vec{u}_{\text{out}} = \dot{R}(\hat{x}\cos 2\alpha + \hat{y}\sin 2\alpha)$ . We then propose the outer velocity field to be the product of its value on the interface and a function of  $\rho$  only. We find that this can indeed fulfill incompressibility if the

droplet is isolated, i.e., if there are no other boundary conditions to be satisfied elsewhere. For the channel geometry, this corresponds to the limit in which the droplet is much smaller than the distance between the walls. The complete solution reads

$$\vec{u}_{\text{in}} = \dot{R}\hat{x}, \quad (11a)$$

$$\vec{u}_{\text{out}} = \dot{R}(\rho_0/\rho)^2(\hat{x}\cos 2\alpha + \hat{y}\sin 2\alpha), \quad (11b)$$

$$R = R(t=0)e^{K't}. \quad (11c)$$

The corresponding streamlines in the outer fluid  $\rho/\rho_0 \propto \sin(\alpha)$ , are circles of different radii tangential to  $y = 0$  and passing through the center of the droplet, although they change into horizontal lines inside it (see Fig. 10 bottom right).

Hence, an off-center circle turns out to be an exact time-dependent solution for any viscosity contrast and independent of it, even beyond the linear regime. For  $A = 1$ ,  $K' = K$  and the filament stretching and the droplet runaway coincide regardless of the droplet shape and whether it is near a filament or not. This single time constant should hence be robust, and indeed an only slightly lower value  $[(0.8-1.0)/t^*]$  is systematically observed in our experiments (squares in Fig. 2). For  $A < 1$ , in contrast,  $K' < K$ , and an isolated, circular droplet has a time constant down to twice smaller (for  $A = 0$ ) than that of the filament stretching. For a droplet connected to the tip of a filament (neither isolated nor circular), we do not know its dynamics rigorously. Our experiments are puzzling in this respect: Isolated droplets (triangles in Fig. 2) and those connected to a filament (circles) display the same growth rate; consistency with the theory then requires it to be  $K'$  (the same than for  $A = 1$ ), since the isolated droplet solution is exact. However, we seem to find a growth rate of  $K$   $[(1.25-1.5)/t^*]$ , and, in any case, higher than the measured value for  $A = 1$ . Our simulations will help clarify this point.

#### D. Stationary-shape solution

The various scaling behaviors derived so far point at an asymptotic pattern enclosing a finite area [Eq. (7); see Fig. 4] with radial, semi-infinite [Eq. (6)] and straight [Eqs. (6) and (5)] filaments of zero width [Eq. (5)] (see Fig. 4) with a droplet at their tip.

In a stationary state,  $\vec{u}_{\text{in}} = \vec{u}_{\text{out}} = 0$  by definition, and the interface shape must balance exactly surface tension with the centrifugal force in Eq. (9):

$$\sigma\partial_s\kappa = \Delta\rho\Omega^2\vec{r} \cdot \hat{s}. \quad (12)$$

Noting that  $\hat{s} = d\vec{r}/ds$ , where  $s$  is arclength along the interface, we can integrate the above equation once to find

$$\kappa(s) = \kappa(s=0) + \Delta\rho\Omega^2/(2\sigma) [r^2(s) - r^2(s=0)]. \quad (13)$$

We see that the curvature of the interface  $\kappa$  increases monotonically with the distance  $r$  to the rotation axis.

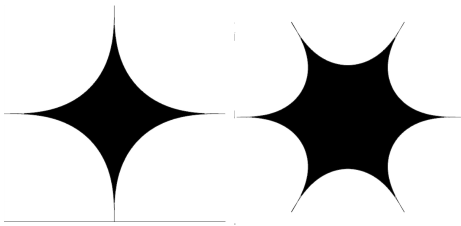


FIG. 4: Stationary solutions in a rotating H-S cell with four- and six-fold symmetry.

In general, the interface will go from convex to concave as  $r$  is increased. The solutions of Eq. (12) which do change concavity do not resemble our observed patterns, but have a petal shape and are unstable [25]. We hence turn to *purely convex* stationary solutions of Eq. (12), up to the point where  $\kappa = 0$ . These will represent the asymptotic incoming fingers. To connect them with the radial, straight filaments, we impose locally radial and straight ends at an arbitrary distance  $r(s = 0)$  from the rotation axis as boundary conditions. Any other connection would cause  $\partial_s \kappa$  in Eq. (12) to diverge.

For given experimental parameters  $\Delta\rho\Omega^2/\sigma$ , this completely determines the solution, an arch covering a certain angle. This angle is a continuous function of the only dimensionless ratio we can construct,  $\Delta\rho\Omega^2 r(s = 0)^3/\sigma$ , and hence only for discrete values of this ratio is the angle a submultiple of  $2\pi$ . This then allows one to connect an integer number of equal arches to form an apparently closed interface, as we show in Fig. 4. This could not be a stationary solution on its own, since actually closing the interface would imply that the arches meet in cusps. We continue each arch end by a straight, semi-infinite radial line, replacing each cusp with an infinite, straight filament of zero width. These filaments present no flux inside (finite velocity but zero width) nor induce any flow outside. They are hence compatible with stationary arches. Finally, the interface is closed by placing a droplet of arbitrary size at the tip of each infinite filament. Although a moving droplet does induce an outside flow around it, this finite disturbance vanishes near the center for an infinite filament.

Thus, we have constructed a solution which shape is stationary at finite distances. Its physical relevance, however, remains to be checked. The slowing down of incoming fingers derived above and the flattening of an initially curved filament  $h(x)$  [Eqs. (6) and (5)] are suggestive that such a solution can indeed be an attractor of the dynamics for initial conditions with the appropriate  $n$ -fold symmetry, and the numerical simulations in next section and the results of Sec. VI further support this idea.

A related issue is the selection of the length scale  $r(s = 0)$  of the stationary arches. For fixed boundary conditions, only discrete values of the dimensionless ratio  $\Delta\rho\Omega^2 r(s = 0)^3/\sigma$  allow equal arches to meet without

crossing. Therefore, for given experimental parameters, the stationary-shape solutions only exist for discrete values of  $r(s = 0)$  (note that unequal arches cannot meet at a *single* distance  $r(s = 0)$  from the center). This sets up a selection problem for the values of  $r(s = 0)$ .

Dynamically, such a solution will be approached with a certain number of fingers. This number may not be unambiguously defined for unequal finger configurations, and it is indeed a dynamic variable for high viscosity contrasts. Furthermore, the initial condition is generically nonsymmetric, with some fingers competing and advancing over others. As a consequence, real experiments and numerical simulations can evolve towards configurations close to the above stationary-shape solutions during a transient but will eventually depart from them. However, for initially equal fingers as those one can produce in simulations (see next section), the dynamics conserve the number of fingers regardless of the viscosity contrast. Hence, only the stationary-shape solution of length scale  $r(s = 0)$  with the number of fingers of the initial condition can be approached. This then unambiguously selects the scale  $r(s = 0)$  and the area enclosed by the stationary interface  $a(t \rightarrow \infty)$  (Eq. 7).

We thus see that the combination of the scaling solutions and the stationary state derived could specify the asymptotic dynamics of equal fingers and the ultimate interface shape. As for its relevance for unequal fingers, we point out two facts: First, we find reasonable agreement between the exponential rate predicted by this simple theory and that measured experimentally for the radial position of the droplets at the tip of the filaments. Second, the existence of the above symmetrical stationary solutions could explain the experimental observation of plateaux in the evolution of the area of inner fluid contained in a reference circle, as a function of time in Ref. [19]. In fact, in those experiments the interface could successively visit the neighborhood of stationary states for different numbers of fingers, and correspondingly slow down the dynamics close to them until some event (typically a pinch-off) would trigger again the dynamics.

## IV. NUMERICAL TESTS

We test the basic picture presented above by phase-field simulations of the full Hele-Shaw dynamics. They are compared to experimental results and to a numerical solution for the stationary arches.

### A. Method

First we adimensionalize the problem: lengths will be measured in units of the initial drop radius  $R_0$ , and time in units of  $t^*$  as given by Eq. (1). All quantities appearing below will be dimensionless. The scaling laws in the previous section can be casted into dimensionless

form just by considering all quantities appearing there dimensionless and redefining  $K = 2/(1 + A)$  and  $K' = 1$ .

The standard Hele-Shaw dynamics is defined by the incompressibility condition already used before ( $\vec{\nabla} \cdot \vec{u}_i = 0$ ), together with the continuity of normal velocities across the interface and the tangential velocity jump [Eq. (9)] as boundary conditions. Thanks to incompressibility, we can define a stream function  $\vec{u} = \vec{\nabla} \times \psi \hat{z}$  (where  $\hat{z}$  is the direction perpendicular to the plates), which is continuous across the interface. We thus obtain the following governing equations [26, 27]:

$$\nabla^2 \psi = 0, \quad (14a)$$

$$\partial_s \psi|_{\text{in}} = \partial_s \psi|_{\text{out}} = -v_n \quad (14b)$$

$$\frac{\partial \psi}{\partial n}|_{\text{out}} - \frac{\partial \psi}{\partial n}|_{\text{in}} = \Gamma, \quad (14c)$$

where the first expresses that the flow is irrotational in each fluid, the second is the continuity of normal velocities, and the third, their tangential jump. The magnitude of this jump is the strength  $\Gamma$  of a divergent vorticity peaked on the interface,  $\Gamma \equiv \gamma + A(\partial_n \psi|_{\text{in}} + \partial_n \psi|_{\text{out}})$ , where  $\gamma/2 \equiv (B\vec{\nabla}\kappa - r\hat{r}) \cdot \hat{s}$  is its local part. We see that the dynamics are controlled only by two dimensionless parameters: the viscosity contrast  $A$  and the dimensionless surface tension  $B = \sigma/[\Delta\rho\Omega^2 R_0^3]$  (the ratio of stabilizing to destabilizing forces). Remarkably, none of the scalings derived in the previous section depends on  $B$ .

Simulations were run using a phase field model presented in [28] and extensively tested in [29]:

$$\epsilon \frac{\partial \psi}{\partial t} = \nabla^2 \psi + A\vec{\nabla} \cdot (\theta \vec{\nabla} \psi) + \frac{1}{\epsilon} \frac{1}{2\sqrt{2}} \gamma(\theta)(1 - \theta^2), \quad (15a)$$

$$\begin{aligned} \epsilon^2 \frac{\partial \theta}{\partial t} &= f(\theta) + \epsilon^2 \nabla^2 \theta + \epsilon^2 \kappa(\theta) |\vec{\nabla} \theta| \\ &+ \epsilon^2 \hat{z} \cdot (\vec{\nabla} \psi \times \vec{\nabla} \theta), \end{aligned} \quad (15b)$$

where  $\theta$  is the phase field, an auxiliary field distinguishing between the two fluids,  $f(\theta) \equiv \theta(1 - \theta^2)$ ,  $\frac{\gamma(\theta)}{2} \equiv \hat{s}(\theta) \cdot (B\vec{\nabla}\kappa(\theta) + \hat{y})$  and  $\kappa(\theta) \equiv -\vec{\nabla} \cdot \hat{n}(\theta)$ , with  $\hat{n}(\theta) \equiv \frac{\vec{\nabla} \theta}{|\vec{\nabla} \theta|}$  and  $\hat{s}(\theta) \equiv \hat{n}(\theta) \times \hat{z}$ .

Apart from the physical control parameters  $A$  and  $B$ , the dynamics in this model also depend on an artificial interface thickness  $\epsilon$  and a relaxation time for the stream function (which is diffusive, not Laplacian)  $\tilde{\epsilon}$ . In the limit  $\epsilon, \tilde{\epsilon} \rightarrow 0$ , the dynamics are strictly those of Eqs. (14a–14c). For finite values of  $\epsilon, \tilde{\epsilon}$ , an error bound is guaranteed for any given magnitude by conveniently decreasing  $\epsilon, \tilde{\epsilon}$  [29].

A very interesting feature of this type of model is that both fluids and the interface between them are treated as bulk. One consequence of this is that the model is well behaved as two interfaces break up and reconnect, which enables us to study the dynamics after pinch-off in a very natural way. This has been demonstrated very

recently [30] for the model used here [28, 29] reformulated in terms of the velocity vector. Let us add a note of caution: When two interfaces approach to distances comparable to their thicknesses  $\epsilon$  (more precisely, below  $5\epsilon$  from numerical tests) they attract each other. This triggers the pinch-off. One could think of this effect as a phenomenological ‘‘pinch rule’’. We nevertheless do not pretend the phase-field dynamics near pinch-off to represent the effect of the third dimension nor the eventual breakdown of a hydrodynamic description. Our approach is to simulate *only* the bidimensional Hele-Shaw dynamics down to distances of  $\mathcal{O}(\epsilon)$ , and continue to simulate them once the reconnected interfaces have separated a distance of the same order, very much as in the experiments, where the Hele-Shaw dynamics can be considered to be accurate before and after the two interfaces were separated a distance of  $\mathcal{O}(b)$ . The crossover from the Hele-Shaw dynamics to interface interaction *via* their finite thicknesses is very abrupt, enabling us to clearly separate one from the other.

For reliable quantitative comparison with theory and experiments, we explicitly check convergence of the time constant  $K$  in  $\epsilon, \tilde{\epsilon}$ , since  $\tilde{\epsilon}$  conveys some finite diffusion time to the flow, and  $\epsilon$  delays the interface advance with respect to the normal fluid velocities [28]. We thus establish exponential rate values for the  $\epsilon, \tilde{\epsilon} \rightarrow 0$  limit, i.e., for the Hele-Shaw dynamics, and bounds for  $\epsilon, \tilde{\epsilon}$  to obtain those values in practice. For  $\tilde{\epsilon}$ , a value of  $\tilde{\epsilon} = 0.5$  turns out to suffice, and it is used in the following unless otherwise stated. Convergence in  $\epsilon$  is discussed case by case.

We numerically integrate the above model with an Euler scheme and centered differences. The time step  $dt$  is taken to be close to the stability limit;  $dt = 0.2\tilde{\epsilon}dx^2$  unless otherwise stated, where  $dx$  is the mesh size. Convergence of the solution is also tested changing  $dx$  ( $dx = \epsilon$  generally suffices as shown in [29]). Our initial condition is some perturbation of a centered circle of unit radius, i.e.,  $r = 1 + \Delta r(\varphi)$  where  $r, \varphi$  are polar coordinates with respect to the rotation axis and  $\Delta r(\varphi) < 1$ . In the next two subsections, we consider only identical fingers ( $n$ -fold symmetry),  $\Delta r(\varphi) = (2\pi/n)q \cos(n\varphi)$ , where  $q$  is the amplitude to wavelength ratio of the perturbation, and  $n$  is the (integer) number of fingers. Unless otherwise stated, we use a dimensionless surface tension  $B$  for which  $n$  is the most unstable mode in the linear regime and  $q = 0.05$ .

## B. Filament thinning

We test here the filament thinning scaling by looking at a dumbbell-shaped pattern: two droplets connected by a filament ( $n = 2$ , see Fig. 5). This case has two advantages: a width can be unambiguously defined as that at the axis of rotation (the midpoint between the two droplets); on the other hand, there are no neighboring filaments to influence its dynamics.



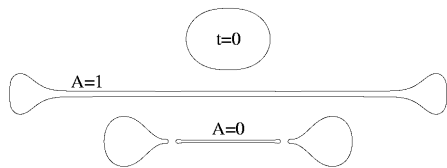


FIG. 5: Filament thinning: Initial condition (top,  $q = 0.05$ ) and one later interface for  $B = 0.09$ ,  $\epsilon = 0.008$ ,  $dx = \epsilon/2$  and  $A = 1$  (middle) or  $A = 0$  (bottom).

Figure 5 displays the patterns thus obtained at the end of our run ( $A = 1$ ) or just after the first pinch-off ( $A = 0$ ). In the last case, new pinch-off events quickly further shorten the central filament from its ends. We will refer to this phenomenon as “pearling”. The two upper curves in Fig. 6 ( $B = 0.09$ ) show the evolution of the filament width at the midpoint for the whole run ( $A = 1$ ) or up to the relaxation of the last central segment in a round shape, which makes the width increase again ( $A = 0$ ). The latter occurs when pearling reaches the rotation axis, shortly after the first pinch-off, indicated by the vertical lines. We see that the asymptotic decay is grossly exponential for  $A = 1$  as predicted, although it is only observed for roughly a decade. For  $A = 0$ , the filament thinning is strictly not exponential since the effective exponential rate varies slowly in time. It should be noticed that it is the flatness, not the width of the filament, what determines the goodness of the approximation of last section. One might think that pinch-off prevents the formation of long and hence straight enough filaments for  $A = 0$ , but, indeed, just before it the  $A = 0$  filament is just as straight as the  $A = 1$  one at the same time; the  $A = 1$  filament already exhibits a clear exponential behavior, whereas the  $A = 0$  one does not.

A closer look reveals that the thinning rate is well relaxed to its asymptotic value for the last third of the run for  $A = 1$ , with a value of  $K = 0.98$  consistent with the predicted  $K$ , but not for  $A = 0$  because pearling reaches the center when the rate begins to approach (from above) a value of  $K = 2$ . No disturbance is observed from the previous pinch-off events. Runs for  $A = 0.5$  and  $A = 0.8$  (not shown) are also in reasonable agreement with the law  $K = 2/(1 + A)$ .

One might blame the high dimensionless surface tension  $B = 0.09$  used or the finite interface thickness  $\epsilon$  or relaxation time  $\tilde{\epsilon}$  in the model for either the slow relaxation of the exponential rate or the pinch-off itself in the low- $A$  case, since  $B$  enters the problem as long as the filament is not perfectly straight. The lower curves in Fig. 6 for a lower dimensionless surface tension,  $B = 0.01$ , and at different values of  $\epsilon$  and  $dx/\epsilon$  rule out both possibilities. Using a more deformed circle ( $q = 0.2$ ), to avoid the appearance of other modes which are linearly unstable, we can confirm the results obtained for  $B = 0.09$ . For high viscosity contrast, the good decay even for the coarsest mesh and interface profile allows to establish the

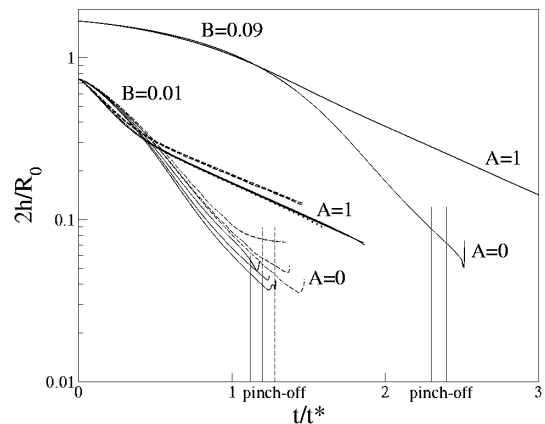


FIG. 6: Filament thinning: Width at rotation axis (in log scale) vs. time. Dashed, solid and dotted line(s):  $dx = \epsilon$ ,  $dx = \epsilon/2$  and  $dx = \epsilon/4$ , respectively. Upper curves ( $B = 0.09$ ):  $\epsilon = 0.008$  (runs in Fig. 5,  $q = 0.05$ ). Lower curves ( $B = 0.01$ ,  $q = 0.2$ ): three curves at  $\epsilon = 0.02$ ,  $0.01$  and  $0.005$  for  $dx = \epsilon$  and three at  $\epsilon = 0.02$ ,  $0.01$ , and  $0.0067$  for  $dx = \epsilon/2$  shown for each value of  $A$ . For  $A = 0$ , lower curves correspond to lower values of  $\epsilon$ . The only  $dx = \epsilon/4$  curve is for  $A = 1$ ,  $\epsilon = 0.02$ . The dashed (solid) vertical lines indicate the interval during which the droplet at the tip pinches off for  $dx = \epsilon$  ( $\epsilon/2$ ).

value of the rate  $K$  unambiguously at  $K = 0.99 - 1.00$  by studying the convergence in  $\epsilon$  and  $dx$ . For low viscosity contrast runs ( $A = 0$ ), the values of the rates again seem to relax towards the end of the runs to a value compatible with the theoretical value  $K = 2$  although they are again badly defined.

Pinch-off is systematically observed for low ( $A = 0, 0.5$ ), but not high ( $A = 0.8, 1$ ) viscosity contrasts. For the latter, a numerical instability due to noise in the (relatively) inviscid fluid often sets in abruptly at late times, especially for the coarser discretization  $dx = \epsilon$ . Because it is so abrupt, it is easy to separate from valid data. For the former, the pinch-off itself cannot be considered a spurious effect due to a finite interface thickness, since the pinch-off time increases only marginally when decreasing the interface thickness  $\epsilon$ , and in any case stays bounded by the vertical lines in Fig. 6. Only for the coarsest interface profile can we detect that the center of the filament anomalously “anticipates” the first pinch-off at its tip; for lower values of  $\epsilon$  it actually continues to narrow unaffected after the first pinch-off and until the subsequent pearling reaches it. Interestingly, when decreasing the mesh size  $dx$  from dashed to solid lines, pinch-off is appreciably accelerated, so that it must also remain in the continuum limit.

We conclude that the theoretical exponential thinning and the values of the exponential rates derived in last section are a good approximation to the observed behavior, especially for high viscosity contrasts. Deviations do exist and are intrinsically much stronger for low viscosity contrasts, but, because they are not less apparent for

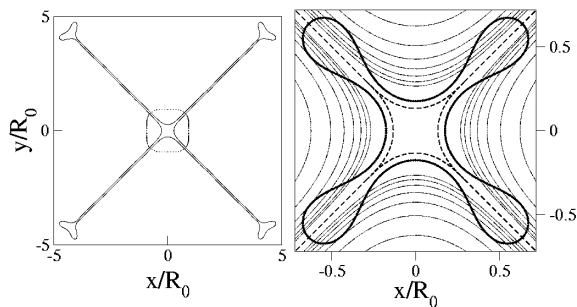


FIG. 7: Approach to the stationary shape for  $B = 0.0213$  and  $\epsilon = 0.01$ . Left: initial (dotted) and latest (solid line) interfaces for  $A = 1$ ,  $dx = 0.5\epsilon$  and  $\tilde{\epsilon} = 0.5$ . Right: Blow-up of central region with intermediate interfaces (solid lines) at constant time intervals. Thicker line: receding interface (after pearling) for  $A = 0$ ,  $dx = \epsilon$  and  $\tilde{\epsilon} = 1$ . Dashed line: numerical solution of Eq. (13) for the predicted stationary shape.

a surface tension almost one order of magnitude lower, they cannot be due to it.

### C. Stationary-shape solution

We now increase the number of fingers arising from the linear regime to  $n = 4$ , so that the incoming fingers enclose a finite area. This enables us to test the approach to the stationary-shape composite solution derived in Sec. III D.

Figure 7 (left) shows the initial condition (dotted line) and the last interface (solid line) of our most refined ( $\epsilon = 0.01$ ,  $dx = 0.5\epsilon$  and  $\tilde{\epsilon} = 0.5$ ) run for  $A = 1$ , just before spurious pinch-off occurs. The latter is unavoidable because the filament width reaches 0.05–0.07, at the edge of diffuse-interface attraction ( $\sim 5\epsilon$ ).  $A = 0$  runs pinch much faster, presumably due to a physical phenomenon and not to the finite interface thickness, since here, as well as for  $n = 2$ , this is not cured by decreasing  $\epsilon$ . Due to this different behavior,  $A = 0$  runs do not lead to the star-like pattern shown here, but, after a first pinch-off event at moderate radii, they quickly emit several droplets while the central drop recedes.

The blowup in Fig. 7 (right) shows the last interfaces for  $A = 1$  at constant time intervals (thinner solid lines) compared to a numerical solution of Eq. (13) for the composite stationary pattern derived in Sec. III D (dashed line). The latter seems a plausible asymptotic solution in the sense that it has not been overcome by the incoming fingers of our run, although visually these seem to asymptotically approach less curved arches. For a quantitative estimate, we fit a slowing down of the type of Eq. (7) [i.e., we fit  $a(t \rightarrow \infty)$ ,  $a(t = 0) - a(t \rightarrow \infty)$  and  $K$ ] both to the time evolution of the area enclosed by a reference circle of various radii  $R_{\text{ref}}$ , and to that of the radial coordinate of the incoming finger tips. We find  $K = 1.06$  for the area enclosed by a circle of radius  $R_{\text{ref}} = 1.25$ , where

the filament begins to look straight, and  $K = 0.9 - 1$  for the incoming finger tip. Both are in good agreement with the theoretical value  $K = 1$ . The area enclosed by smaller circles decays with smaller exponents (0.93 for a circle of radius  $R_{\text{ref}} = 1$  and 0.81 for  $R_{\text{ref}} = 0.75$ ), but a worse agreement is understandable, since the filaments are less straight at the latest times we can explore.

Regarding the tip of the incoming fingers and the total enclosed area in the center, the numerical solution of Eq. (13) predicts  $r_{\text{min}} = 0.133$  and  $a(t \rightarrow \infty) = 0.0937$  respectively. The numerical simulations here presented show that the filament still contains a significant amount of inner fluid, yielding an asymptotic enclosed area which decreases with the radius of the reference circle ( $a(t \rightarrow \infty) = 0.36$  for  $R_{\text{ref}} = 1.25$ ,  $a(t \rightarrow \infty) = 0.27$  for  $R_{\text{ref}} = 1$  and  $a(t \rightarrow \infty) = 0.20$  for  $R_{\text{ref}} = 0.75$ ). As for the asymptotic tip position of the incoming fingers, we find  $r_{\text{min}} = 0.2$ , with little sensitivity to the time window used. We thus seem to find that the tips and the area enclosed reach roughly half of those predicted by Eq. (13). This mismatch is most probably due to the fact that we do not yet probe close enough to the stationary-shape solution. This is indeed the case regarding the filaments since, as explained above, they have not reached its zero-width asymptotic state because the final area is not independent of the reference circle radius (as it should be if  $R_{\text{ref}} < r(s = 0)$ ).

However, the evolution of the interface for  $A = 0$  after pinch-off does hint that this exact solutions have an important effect on the dynamics. After the pearling process of the filaments for  $A = 0$ , the incoming fingers continue to approach the rotation axis and the droplets left at the tip of the filaments recede. When they reach the central region roughly delimited by the ends of the arches of our predicted stationary-shape solution, surface tension finally stops the advance of the incoming fingers. The whole drop left at the center relaxes towards a circular shape. The thicker solid line in Fig. 7 (right) corresponds to such a central shape at the time when the incoming fingers stop before the relaxation to a circular shape. Although the shape displayed is not an asymptotic one, the remarkable resemblance of the tip of the incoming fingers and the steady-state asymptotic arches (dashed lines) and the fact that incoming fingers precisely stop (their velocity crosses zero) when approaching this shape is suggestive that our steady-shape solution (or parts of the solutions found in [25] very similar to it) is indeed the attractor for sets of initial conditions with  $n$ -fold symmetry.

### D. Unequal finger dynamics

Finally, we address the more realistic case of unequal fingers. The goal here is no longer to test our theoretical results, but to directly compare with experimental patterns. We thus check whether the differences between low and high viscosity contrasts  $A$  observed in experi-

ments, including systematic or not pinch-off events, can be explained by the Hele-Shaw equations.

In order to compare with the patterns shown in Fig. 1, which have 15–16 filaments for  $A = 1$  [Figs. 1(a,b)] and 20–21 for low  $A \sim 0.45$  [Figs. 1(c,d)], we use a dimensionless surface tension of  $B = 1.03 \times 10^{-3}$ , which corresponds to a most unstable mode  $n = 18$ . The idea is to use exactly the same initial condition and physical and computational parameters for both low and high viscosity contrast  $A$ , except for  $A$  itself. Thus, any difference we observe can only be due to the different values of  $A$ .

We adopt the less refined choices  $dx = \epsilon$  and  $\tilde{\epsilon} = 1$  with an interface thickness down to  $\epsilon = 0.005$ , in order to avoid possible spurious pinch-off events. As already observed for the dumbbell-shaped pattern in Sec. IV B, we find that, whenever pinch-off occurs, a lower rate of  $dx/\epsilon$  does not prevent it, but even accelerates it.

As for the initial condition, if we start with a perturbation where sine and cosine modes have uniformly or Gaussian distributed random amplitudes up to a certain cut-off (here  $n = 40$ ), we cannot reproduce the strong asymmetry of the experimental patterns for high viscosity contrast  $A = 1$  [Figs. 1(a,b)]. We traced this back to the fact that, in the experiments, the deviations from a circle first become visible in particular spots, and not uniformly on the interface. For the experiment of Figs. 1(a,b), this happens roughly on three spots. We mimic this by multiplying our random initial condition by an exponential envelope peaked at three uniformly distributed random angles, keeping  $\Delta r(\varphi) \leq 0.004$ . We do not attempt to truly copy the experimental initial condition, but to use a somehow “statistically” similar one.

If some details look alike, these will then indicate some general common trends representative of the dynamics, as opposed to a particular initial condition.

This initial asymmetry in the deviations from a circle is largely preserved throughout the whole evolution for high [ $A = 1$ ; Figs. 8(a,b)], but not low viscosity contrast [ $A = 0, 0.5$  runs; Figs. 8(c,d) and Figs. 8(e,f), respectively]. We hence conclude that both an asymmetric initial condition and a high viscosity contrast are necessary to obtain asymmetric patterns. This effect of the viscosity contrast is due to the incoming finger competition for high  $A$ , although it is less apparent here than in the channel geometry, due to the geometric decrease of available room fingers experience.

Figure 8 is indeed the simulation analogue of Fig. 1. Experimental patterns in Fig. 1 were rotated at will to make the “statistical” resemblance with the simulations more apparent; simulations are presented with the vertical and horizontal directions parallel to the computational grid, although lattice anisotropy is not appreciable here.

Patterns are shown at two different times:  $t = 1.32$  [Figs. 8(a,c,e)] and  $t = 1.74$  [Figs. 8(b,d,f)], for all viscosity contrasts. Rather than comparing these simulations with experiments at equal dimensionless times, we

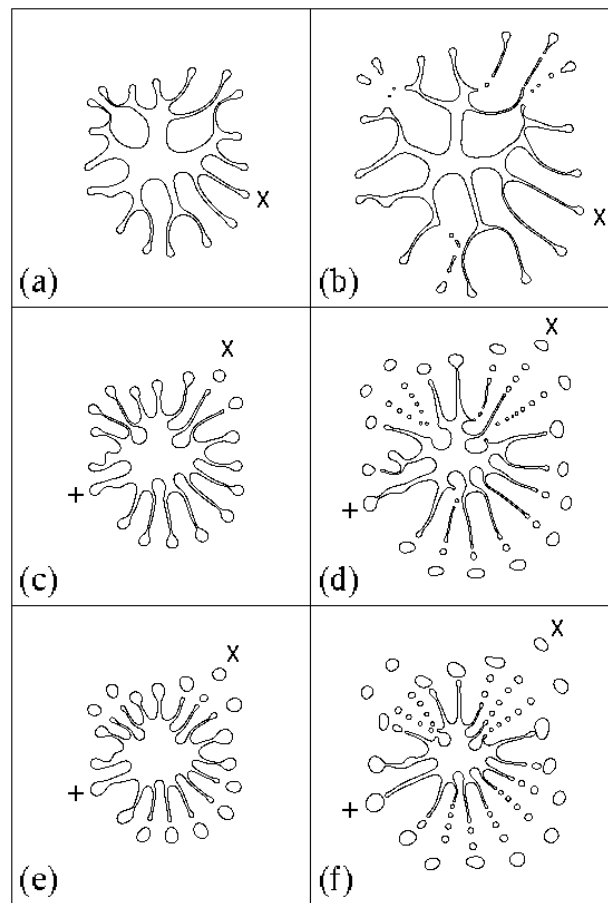


FIG. 8: Pattern evolution for a random initial condition (see text) and  $B = 1.03 \times 10^{-3}$ ,  $\epsilon = 0.005$ ,  $dx = \epsilon$ ,  $\tilde{\epsilon} = 1$  and  $A = 1$  (a,b),  $A = 0.5$  (c,d) or  $A = 0$  (e,f). Snapshots ( $3R_0 \times 3R_0$ ) shown at  $t = 1.32$  (left) and  $t = 1.74$  (right).

present all the patterns when their envelope has roughly attained twice [Figs. 1(a,c) and 8(a,c,e)] and three times [Figs. 1(b,d) and 8(b,d,f)] the initial circle radius. Direct comparison of the time scales is left for Sec. V.

Let us first compare patterns at the earlier stage [Fig. 1(a) with Fig. 8(a), and Fig. 1(b) with Fig. 8(b)]. The similarity between experiments and simulations is remarkable, especially if one takes into account that the initial conditions were only “statistically” similar (see above). Furthermore, the common features (overall morphology, filament accomplished or frustrated branching, droplet size, the already mentioned incoming fingers) are well reproducible in other simulation runs and experiments. This all indicates that the excellent agreement in the typical morphologies between experiments and simulations is not fortuitous. This is noteworthy, since a change in the wetting conditions for the high viscosity contrast experiments, for instance, completely changes the observed morphology [20].

From this earlier stage it would seem that pinch-off is not significantly more present for the lower ( $A = 0.5$ )

than higher ( $A = 1$ ) viscosity contrasts. However, simulation offers us the possibility to go to the ideal limit  $A = 0$ , in which both fluids have strictly equal viscosities. Fig. 8(e) shows that most droplets have pinched-off by the same time for  $A = 0$ . Comparing Figs. 8(a,c,e) between them, it is clear that pinching arises as the viscosity contrast is decreased.

Another possibility is to go to later times. The experiments still show no pinch-off for  $A = 1$  [Fig. 1(b)], but most filaments have emitted at least one droplet for  $A \simeq 0.5$  [Fig. 1(d)]. The simulations would seem less conclusive, since they display some pinch-off events for  $A = 1$  [Fig. 8(b)]. However, these are most likely to be spurious: They occur for very narrow filaments, whose width is comparable to the interface thickness  $\epsilon$ , and we know from earlier work [28, 29] that overlapping diffuse interfaces attract each other. Most importantly, pinching is inhibited as  $\epsilon$  is decreased (the same run with a larger value of  $\epsilon$  displays more pinching).

Simulations for low viscosity contrasts [ $A = 0.5$ , Fig. 8(d) and  $A = 0$ , Fig. 8(f)], show much more pinching (the lower  $A$ , the more). The first pinch-off at the tip of a filament does not significantly change with  $\epsilon$ , very much like we observed for the dumbbell-shaped pattern in Sec. IV B. Some pinch-off events disappear, while other appear; some are reentrant in  $\epsilon$  (they disappear for a middle value of  $\epsilon$  but reappear when  $\epsilon$  is further decreased). We hence conclude that these first pinch-off events are *not* spurious. In any case, longer and thinner filaments are achieved as  $\epsilon$  is decreased.

Pearling (successive pinch-off events shortening a filament from its outer end) is *increased* when decreasing  $\epsilon$ , even though it is less present in the experiments [Fig. 1(d)]. It is interesting to note the absence of pinching at the base of the filaments, near the rotation axis, for  $A = 0$  [Fig. 8(f)], as opposite to the  $A = 0.5$  and  $A = 1$  runs [Figs. 8(b,d), respectively]. Since we saw pinching to be spurious for the  $A = 1$  run, this suggests that such events at the base of a filament are also spurious. Furthermore, they are not observed in the experiments.

We conclude that simulations reproduce very accurately the experimental morphologies before pinching, which strongly supports the idea that the dynamics can be considered to be the standard Hele-Shaw for that purpose. They also indicate that these bidimensional dynamics do lead to finite-time pinching for low, but not high viscosity contrasts. The crossover occurs somewhere between  $A = 0.5$  and  $A = 1$ .

### E. Filament stretching and droplet dynamics

We have postponed the study of the filament stretching and droplet scalings to present it in a unified way, for all the cases ( $n = 2, 4$  and 18 filaments) considered above. Let us first summarize what we can expect from the theory in Sec. III: Droplets at the tip of a filament should run away roughly exponentially in time, with a

rate comprised between  $K' = 1$  (for an isolated droplet) and  $K = 2/(1 + A)$  (the filament thinning rate). The lower bound  $K'$  corresponds to the idealized case where the filament does not perturb the droplet shape nor the flow created by it, so that the droplet still obeys the exact solution for an isolated and circular one. This assumption is more realistic for high viscosity contrasts, since we have seen that in the  $A \rightarrow 1$  limit the homogeneous flow inside an isolated circular droplet holds for any closed interface, regardless of its shape and whether it is isolated or not. Note, however, that a droplet at the tip of a filament is not completely closed, so that a deviation from  $K'$  is still possible.

The upper bound  $K$  is based on another idealization, where no fluid is fed into the droplet, so that all the fluid expelled by the filament as it narrows is used to extend it. Therefore, the radial coordinate of the neck of the filament just before the droplet scales with the same exponent  $K$  as the filament width. If the shape of the droplet is stationary, the radial coordinate of the droplet center of mass is then just that of the neck of the filament plus a constant.

The purpose of this section is to determine which is the actual evolution of the radial coordinate of the droplets center of mass. Our experiments have not clearly answered this question: Droplets are seen to (i) run away with roughly the same rate whether connected to a filament or isolated, but (ii) this observed rate seems to be  $K$  (filament thinning) rather than  $K'$  (isolated droplet). The problem is that (ii) is inconsistent with the *exact* isolated droplet solution.

Fig. 9 shows the evolution of the radial coordinate of a droplet center of mass for the dumbbell-shaped pattern in Fig. 5 ( $n = 2$ , dashed lines) and some of the furthest droplets in Fig. 8 ( $n = 18$ , solid lines), compared to that of an isolated circular droplet ( $n = 1$ , dotted lines). Bold (thinner) lines correspond to  $A = 1$  (0). Curves are shown till the end of the respective runs, except for the isolated droplet, which is shown only until it begins to “feel” the finite simulation box. Note that for  $n \geq 2$  curves make little sense for  $R < R_0$ , and this part has been removed for the  $n = 18$  runs, since the code actually detected a different droplet at those early stages. More details on how the curves were obtained can be found below. Although the range of  $R/R_0$  monitored decreases with increasing  $n$ , the final aspect ratio of the pattern (droplet radius to length of filament for  $n \geq 2$ , or droplet radius to radial coordinate of center of mass of the isolated droplet) attained is similar.

Clearly, all droplets scale with roughly the same rate  $m$ , although runs with  $A = 1$  show a good linearity, whereas those for  $A = 0$  do not. More precisely, for  $A = 1$  (0), one measures (in the straightest segment of the curves)  $m = 0.8$  (0.7) for  $n = 2$ ,  $m = 0.82$  (0.75) for  $n = 18$ , and  $m = 0.88$  (0.83) for  $n = 1$ . Runs for  $n = 4, 6, 8, 11$  and 12 fingers, give similar results, also for intermediate values of the viscosity contrast ( $A = 0.5, 0.8$ ).

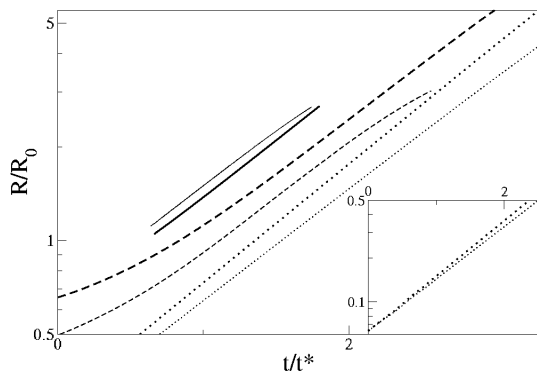


FIG. 9: Radial position (in log scale) of the center of mass of various droplets vs. time, for  $A = 1$  (bold) and  $A = 0$  (thinner curves). Solid, dashed and dotted lines correspond to the droplets indicated with an “x” in Figs. 8(a,b,e,f), those in Fig. 5, and the isolated droplet in Fig. 10 bottom-right, respectively. Curves are shown till the end of the respective runs, except for the isolated droplet, which is shown only until it begins to “feel” the finite simulation box. Inset: Linear regime of the isolated droplet, continued in the main plot after translating the (dotted) curves to earlier times for comparison with the others. The inset preserves slopes with respect to the main plot.

Since all droplets scale with a same rate, roughly independent of  $A$  and close to  $K' = 1$ , it is clear that the droplet scaling is dominated by that of an isolated droplet. This rate is found to be insensitive to pinch-off, and it also holds for the experimental isolated droplet in Fig. 9 (dotted lines), which further supports this idea, and confirms this part of our experimental conclusions (i). However, the fact that droplets scale roughly with  $K' = 1$  for any viscosity contrast  $A$  in our simulations ( $m \sim 0.8$ ) and certainly not with  $K = 2/(1+A)$  confirms that there is some problem with the statement (ii) that the experimental growth rate be  $K = 2/(1+A)$ , as already expected from the exact isolated droplet solution. We address this issue in the following section.

The mismatch between the droplet scaling ( $m \sim 0.8$ ) and the filament thinning  $K = 2/(1+A)$  accounts for the fluid fed into the droplet. This is relatively small for  $A = 1$  ( $K = 1$ ), but not for  $A = 0$  ( $K = 2$ ). This explains the experimental and numerical observation that droplets grow faster and larger as  $A$  is decreased. The bad linearity of the  $A = 0$  runs is also probably due this large mismatch, although we recall that the filament thinning itself displays a less constant exponent for  $A = 0$  than  $A = 1$ .

The center of mass of the droplets for  $n = 2, 18$  in Fig. 9 was computed subtracting the final droplet radius to the droplet tip position, which is not rigorous, because the droplet radius changes during the evolution. However, if one subtracts, say, the final distance from the droplet tip to the neck of the filament before the droplet for comparison, rates increase by 0.1 only (not shown).

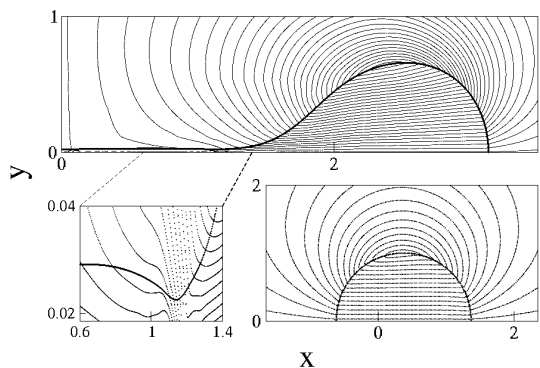


FIG. 10: Stream lines induced for  $A = 0$  by a dumbbell-shaped pattern as that in Fig. 5 (top; a quarter of the interface shown,  $B = 0.09$ ,  $\epsilon = 0.0067$ ,  $dx = \epsilon/2$ ,  $\tilde{\epsilon} = 0.5$ ) or by an off-center circular droplet (bottom right; a half shown,  $B = 0.32$ ,  $\epsilon = 0.02$ ,  $dx = \epsilon$ ,  $\tilde{\epsilon} = 0.1$ ,  $dt = 0.25\tilde{\epsilon}dx^2$ ). Bottom left: Blow-up ( $y$  enlarged 30 $\times$  more than  $x$  coordinate) of the forming neck in the top pattern. Interface (thicker lines) and contour plot of the stream function (thinner lines) at equally spaced levels (different in each graph);  $x = y = 0$  is the rotation axis.

We have also extracted the neck position (not shown) of the same droplets (marked with an “x”) in Fig. 8, and measured an exponent up to  $m = 0.9$  (for  $A = 0.5$ ). We also confirmed that a droplet which pinches only at the end of the run (marked with “+”) scales with the same rate than one of the first to pinch (marked with “x”).

In the end, the main effect of the filament on the scaling of the center of mass of the droplet seems to come from the injection of inner fluid into it, rather than perturbing the droplet environment. This should mean that the flow of the inner fluid is much more affected than that of the outer by the presence of the filament. The latter is illustrated for the most sensitive case ( $A = 0$ ) in Fig. 10, where stream lines are superimposed to the interface for a quarter of a dumbbell-shaped pattern (top), as that in Fig. 5, and for half an isolated droplet (bottom right): The most remarkable difference is the higher density of stream lines (higher velocity) at the entrance of the droplet and *inside* it, which breaks the flow uniformity within the droplet; the outer flow is qualitatively similar near the droplet (note that stream lines are not shown at the same levels for a maximum resolution of the flow details in both cases, so that the modulus of the velocity cannot be compared).

When a neck is formed (blowup, bottom left, in Fig. 10), the flow is affected also outside the droplet, but mostly near the neck. Because pinching then also occurs in a time scale sensibly shorter than that of the filament stretching, the effect is not perceived in the latter. The  $A = 0$  droplets tracked in Fig. 9, for instance, pinch during  $t \in (0.9, 0.96)$  for  $n = 18$  and  $t \in (2.3, 2.4)$  for  $n = 2$ , but they curve down well after or before it, respectively.

One could also wonder why the exponents measured for the isolated droplet run are not strictly  $m = K' = 1$ ,

but this is certainly a finite-interface-thickness correction due to the less refined value used ( $\epsilon = 0.02$ ). Our purpose here was merely to check that the exact solution for the isolated droplet has some finite basin of attraction, as we find it to be the case: The droplet stays circular and runs away exponentially with a very steady rate from the linear ( $q = 0.005$ , inset of Fig. 9) to deep into the nonlinear (main plot) regimes. The droplet depicted in Fig. 10 bottom right corresponds to the end of the linear (and beginning of the nonlinear) regime. The type of flow predicted by the exact solution [Eqs. (11)], is apparent here.

## V. TIME SCALE

In Sec. IV E we saw that the statement that the experimental growth rate be  $K = 2/(1+A)$  and not  $K' = 1$  is inconsistent not only with the exact isolated droplet solution, but also with numerical simulations of the Hele-Shaw equations. This statement relies only on the observed  $A = 0.45$  rates, since for  $A = 1$   $K = K' = 1$  (in good agreement with the measured values). This indicates that our experiments for low  $A$  do not follow the standard Hele-Shaw dynamics.

A three-dimensional study of the proper effective boundary conditions to apply on an idealized two-dimensional interface, as performed for air displacing a liquid [31], is lacking for the case of two liquids. This low- $A$  case might be different, since a second viscosity is involved when a layer of vaseline oil (outer fluid) wets the plates also inside the silicone oil (inner fluid) domain. Note that, for  $A = 1$ , such a wetting layer (in this case, of silicone oil) is to be found in the air. However, different boundary conditions should in general not produce experimental patterns so similar to the outcome of simulations using standard boundary conditions as those in Sec. IV D. Especially, they should not necessarily preserve the pinch-off for low  $A$ .

The inferred dimensionless rates for the experimental droplet runaway rely on the measured rates and on the time scale  $t^*$ . A modification of the latter can hence already account for the observed discrepancy between theory and simulations. To further realize this, it is instructive to compare again experimental (Fig. 1) and simulation (Fig. 8) patterns: The similarity in the morphologies is obvious, but time scales are not straightforward to compare, since the degree of deviation from a perfect circle in the experimental initial condition is unknown. This results in an effective “latency time”, during which no significant departure from a circle is observed.

However, we can compare the time elapsed for the pattern envelope to grow from a radius of  $2R_0$  [Figs. 1(a,c) and 8(a,c,e)] to  $3R_0$  [Figs. 1(b,d) and 8(b,d,f)]. This is  $\Delta t = 6\text{s}(36\text{s})$  for  $A=1(0.45)$  in the experiments. With the measured values of the physical parameters,  $t^*$  in Eq. 1 is  $t^* = 15.5\text{s}(134\text{s})$ , which results in a dimensionless time interval  $\Delta t/t^* = 0.39(0.27)$  for  $A=1(0.45)$ . This is to

be compared with  $\Delta t/t^* = 0.42 \forall A$  in the simulations. The mismatch between experiments and simulations is not significant (taking into account the viscosity uncertainty and the subjectivity in the snapshots to compare) for  $A = 1$ , but it is for  $A = 0.45$ . This is just a (statistical) confirmation of the droplet scaling, since it is this scaling what determines the growth of the pattern envelope, but makes it clear that the main difference between experiments and simulations is the time scale for  $A = 0.45$ .

A simple explanation is that the vaseline wetting layer has a more obvious effect than modifying the effective two-dimensional boundary conditions on the interface: it changes the expression for Darcy’s law [Eq. (8)]. The two-dimensional velocity in Darcy’s law results from an average over the cell gap of the three-dimensional velocity field. We simply point out that one should average over the fraction of the gap actually filled with silicone oil when computing the averaged silicone oil velocity. Assuming stick boundary conditions for the vaseline on the glass plates, and no-slip between vaseline and silicone, we average the silicone velocity in a region closer to its maximum (at the midplane between the two glass plates) than in the absence of the vaseline wetting layer. This results in a higher velocity, further enhanced by the fact that vaseline is less viscous. More precisely, we find

$$\vec{u}_{\text{in}} = -\frac{b^2[1 + \Delta b^2]}{12\mu_{\text{in}}}(\vec{\nabla}p_i - \rho_i\Omega^2 r\hat{r}), \quad (16)$$

where

$$\Delta b^2 = \frac{2w}{b} + \left(8 + 6\frac{\mu_{\text{in}}}{\mu_{\text{out}}}\right)\left(\frac{w}{b}\right)^2, \quad (17)$$

with  $w$  the thickness of the vaseline wetting layer at each glass plate. The effect of this on the time scale of the dynamics  $t^*$  in Eq. (1) is to replace  $\mu_{\text{in}}$  there by  $\mu_{\text{in}}/[1 + \Delta b^2]$  ( $\vec{u}_{\text{out}}$  stays unchanged). For a wetting layer of thickness  $w$  10% of the total cell gap  $b$ , our  $A = 0.45$  time scale should decrease by a factor 0.78. This resets the rate at which droplets run away to  $m = 0.97-1.17$ , in reasonable agreement with theory and simulations. We have not measured the thickness of the wetting layer  $w$ , and possibly other effects like the effective two-dimensional boundary conditions on the interface might play a role, but this gives a plausible explanation of our observations.

## VI. LUBRICATION THEORY

The purpose of this section is to derive the time evolution of a gently curved filament in a more systematic way. In particular, we would like to account for the striking difference between the filament thinning of high and low viscosity contrast dynamics.

To do so, we perform a lubrication approximation for the interface. This assumes the interface height  $h(x, t)$

in Fig. 3 to vary in a scale  $\Delta h$  much smaller than the scale of horizontal variations  $\ell$ , and expands formally all quantities in powers of  $\varepsilon = \Delta h/\ell$ . We then find an evolution equation for  $h$  up to first order in  $\varepsilon$ . The idea is to see whether the viscosity contrast can affect the relative importance of the various terms and to what order it enters.

We begin by rewriting the free boundary problem of Eqs. (14) into an exact evolution equation for  $h$ : Using the vortex-sheet formalism of Refs. [26, 32], we have

$$\partial_t h = U_{\hat{y}} - U_{\hat{x}} h_x, \quad (18)$$

where  $U(x, t) = U_{\hat{x}} \hat{x} + U_{\hat{y}} \hat{y}$  is the mean fluid velocity at the interface, which we assume to vary only in the  $x$  direction:

$$\begin{aligned} \vec{U}(x, t) = & \frac{1}{2\pi} P \int_{-\infty}^{+\infty} \frac{(h(x') - h(x), x - x')}{(x - x')^2 + (h(x') - h(x))^2} \Upsilon(x') dx' \\ & - \frac{1}{2\pi} P \int_{-\infty}^{+\infty} \frac{(-h(x') - h(x), x - x')}{(x - x')^2 + (h(x') + h(x))^2} \Upsilon(x') dx', \end{aligned} \quad (19)$$

where  $P$  is the Cauchy principal part and  $\Upsilon = \Gamma(1 + h_x^2)$  ( $\gamma$  defined in Sec. IV A) becomes

$$\Upsilon/2 = B \partial_x \kappa - A \vec{U} \cdot (\hat{x} + \hat{y} \partial_x h) + x + h \partial_x h. \quad (20)$$

We now scale  $h$  with  $\Delta h$ ,  $x$  with  $\ell$ , and the interface velocity  $\vec{U}$  with  $V_0 = (B/\ell^2) + \ell$ . We expand any quantity  $Q$  as  $Q = Q^{(0)} + \varepsilon Q^{(1)} + \varepsilon^2 Q^{(2)}$ , so that the evolution equation for  $h$  up to  $O(\varepsilon)$  becomes

$$\partial_t h = U_{\hat{y}}^{(1)} - \partial_x h U_{\hat{x}}^{(0)} + \varepsilon (U_{\hat{y}}^{(2)} - \partial_x h U_{\hat{x}}^{(1)}), \quad (21)$$

where we have anticipated that  $U_{\hat{y}}^{(0)} = 0$ .  $\vec{U}$  and  $\Upsilon$  are indeed expanded along the same lines as in Refs. [14, 32], to further find

$$U_{\hat{x}}^{(0)} = \frac{1}{2} \Upsilon^{(0)} \quad U_{\hat{x}}^{(1)} = \frac{1}{2} \Upsilon^{(1)} + H[\partial_x (h \Upsilon^{(0)})] \quad (22)$$

$$U_{\hat{y}}^{(1)} = -\frac{1}{2} [\partial_x (h \Upsilon^{(0)}) + h \partial_x \Upsilon^{(0)}] \quad (23)$$

$$U_{\hat{y}}^{(2)} = -\frac{1}{2} [\partial_x (h \Upsilon^{(1)}) + h \partial_x \Upsilon^{(1)} - h H[\partial_x^2 (h \Upsilon^{(0)})], \quad (24)$$

$$\Upsilon^{(0)} = \frac{2L}{(1+A)V_o} \eta(x) x \quad (25)$$

$$\Upsilon^{(1)} = \frac{2B}{(1+A)V_o L^2} \partial_x^3 h - \frac{2A}{1+A} H[\partial_x (h \Upsilon^{(0)})], \quad (26)$$

where  $H(x) = \pi^{-1} P \int_{-\infty}^{+\infty} f(x') dx' / (x - x')$  is the Hilbert transform of  $f(x)$ , and  $\eta(x)$  is an arbitrary cut-off function in the centrifugal force to render  $H$  finite, which is 1 up to a certain distance  $x_F$  and then decreases to zero in

an arbitrary way. We pursue the calculation and check whether the result is independent of the shape of  $\eta$ . This cut-off is necessary, as opposed to the channel case, because the zero order of the vorticity in a rotating cell is neither zero nor a constant but,  $\Upsilon^{(0)} \propto x$ . The other major difference between the weakly nonlinear expansion performed in [32] and this lubrication approximation is the appearance of the second integral in (19). Its expansion is not trivial as pointed out in [14]; there it was solved using limiting procedures, the Plemelj formula, and delta function representations.

Substituting these results into Eq.(21), undoing only the scaling of the velocity, and dropping the cut-off function  $\eta(x)$ , which is not necessary for finite or asymptotically straight infinite filaments, we finally obtain

$$\begin{aligned} \frac{1+A}{2} \partial_t h = & -\partial_x (xh) - \varepsilon B \partial_x (h \partial_x^3 h) \\ & - \varepsilon \frac{(1-A)}{1+A} \partial_x (h H[\partial_x (xh)]). \end{aligned} \quad (27)$$

We see that this is a simple continuity equation for  $h$ , namely that already used in Sec. III A,  $\partial_t h = -\partial_x (h v_{\hat{x}})$  [Eq. (2)], but now with an inner fluid velocity along the  $x$  direction

$$v_{\hat{x}} = \frac{2}{1+A} \left( x + \varepsilon B \partial_x^3 h + \varepsilon \frac{1-A}{1+A} H[\partial_x (xh)] \right) \quad (28)$$

which is no longer just  $v_{\hat{x}} = Kx$  as used in Sec. III B, but takes into account all the terms entering the tangential velocity jump there [Eq. (9)].

We now present a general solution when the order  $\varepsilon$  in Eq.(27) is neglected. Any given initial condition  $h_0(x)$  evolves following a simple scaling  $h(x, t) = L h_0(Lx)$  [Eq. (3)] with  $L = e^{-Kt}$  and  $K = 2/(1+A)$ . This agrees with the scaling found in Sec. III A for an initially straight interface. Here, we find that the result is more general and, as a consequence, any interface approaches zero at least at infinite time. In this way, rotation produces pinch-off at infinite time independently of the initial interface. This is to be compared with the influence of a gravity jet which only produces a shift in the moving frame.

This leading behavior smooths out the gradients both by lowering height differences [Eq. (5)] and by stretching neighboring points apart [Eq. (6)]. One would expect straight filaments to be stable, and the solution to become increasingly accurate in time. This smoothing effect of the centrifugal force through the zeroth order term  $v_{\hat{x}} = Kx$  presumably competes with the higher order terms: The term in dimensionless surface tension  $B$ , for instance, is known to lead to finite-time pinch-off in the absence of any other force and for an inviscid outer fluid ( $A = 1$ ), for certain initial conditions [10, 11, 14]. The analysis of the interplay between rotation and surface tension and their competing effects deserves an in-depth separate analysis that will be carried out elsewhere.

However, we can address in this framework the systematic observation of pinch-off events in experiments and

simulations for low viscosity contrasts  $A = 0\text{--}0.5$  and the lack of them for high viscosity contrast. This fact cannot be explained by the two first terms in the r.h.s of (27). If such singularities and differences are contained in the Hele-Shaw dynamics as the simulations seem to indicate, they should be linked to the remaining non local term of order  $\varepsilon$ . Although this term does indeed play a role for  $A < 1$ , we have seen that it enters at the same order than the surface tension term. The question is then how this, in principle, higher order term can affect the general asymptotic scaling of filaments which typically become straight for any viscosity contrast.

The answer is in the *non-local* nature of the new term. Hence, a locally straight filament is still influenced by a curvature elsewhere. Real filaments are finite, and this means that the upper and lower interfaces necessarily meet in a highly curved region (in practice, a droplet at the tip), where the  $\varepsilon$  expansion breaks down. Because this will be felt by an elsewhere straight filament, the  $\varepsilon$  expansion is much more delicate for low viscosity contrast, and significant deviations from the scaling of Eqs. (3) or (5) can be expected. The influence of a curved region decays with distance, so that these deviations should decay for the central part of a filament as it grows long enough for its ends to have little effect on it.

Although it is difficult to address the precise effect of the non-local term analytically, we can gain some insight by considering the simplest possible situation: a perfectly straight filament of time-dependent arbitrary width. More precisely, we consider only an upper straight interface given by  $y = h(t)$  in Fig. 3 and the region  $y > 0, x > 0$ , with no-flux boundary conditions on the axis  $y = 0$  and  $x = 0$ , exactly as in our simulations in Sec. IV B. Proposing a stream function  $\psi$  (bi)linear in  $x$  and  $y$  to solve the full Hele-Shaw equations [Eqs. (14)], we find

$$\psi_{\text{in}} = K_{\text{in}}xy, \quad (29a)$$

$$\psi_{\text{out}} = h(K_{\text{in}} - K_{\text{out}})x + K_{\text{out}}xy, \quad (29b)$$

$$h = h(t=0)e^{-K_{\text{in}}t}, \quad (29c)$$

$$K_{\text{in}} = K + \frac{(1-A)}{1+A}K_{\text{out}}, \quad (29d)$$

where we recall that  $K = 2/(1+A)$ .

For  $A = 1$ , we recover  $K_{\text{in}} = K$  because the inner fluid and interface dynamics are completely specified and decoupled from the outer flow. For  $A < 1$ , however, the whole solution depends on the outer flow, and hence on actual external boundary conditions. For a semiinfinite filament and no *external* breaking of the translational symmetry,  $K_{\text{out}} = 0$ , and the scaling solution is again valid and exact.

For a finite filament, though, there will necessarily be a recirculation (not to speak of the flow created by a droplet): Stream lines going out of the filament at its tip will come back to different points of the interface, in a loop of the size of the filament length  $R$  itself. The outer flow solution proposed will no longer be valid, but, for

a long enough filament, we can assume that the solution still holds for  $x \ll 1$ . Given the fact that recirculation requires a positive hyperbolic profile close to the origin (see Fig. 10),  $K_{\text{out}}$  must be positive and therefore  $K_{\text{in}} > K$ , slowly approaching  $K$  as the filament grows longer. This is consistent with the filament thinning exponent for  $A = 0$  observed in Fig. 6.

One could speculate that this effect becomes stronger as one approaches the filament tip (although the flow also looks different), making the local, effective thinning (and its rate) increase. This would lead to the formation of a more shallow region (the neck) and thus initiate the pinch-off. The forming neck then happens to receive a much higher density of incoming stream lines that its vicinity (see Fig. 10, blowup at the bottom left), pushing it further down. Surface tension enters the problem as the filament is locally curved, so that it is not possible to tell whether the pinch-off itself is due to the non-local term or to surface tension, or yet to a combination of the two unless a careful analysis is performed. It is nevertheless clear that the non-local term does provide the initial departure from the scaling solution needed to overcome its smoothing effect.

## VII. DISCUSSION AND CONCLUSIONS

We have studied viscous fingering in a rotating Hele-Shaw cell from the point of view of the dynamical approach to pinch-off singularities. We have found that this is linked to a global scaling of the pattern: Radial filaments of denser inner fluid narrow and stretch; they push away the droplet at their tip, and incoming fingers of less dense, outer fluid approach the rotation axis to compensate for the flux expelled through the filaments. For  $n$ -fold symmetric patterns, the system can approach either a steady shape in infinite time or a finite-time pinch-off singularity. The former consists of  $n$  convex arches ending in straight, formally semiinfinite radial filaments of zero width with a droplet at their tip (at infinity) connecting each pair of arches and running away with infinite velocity.

Thus, we see that rotation enforces pinch-off as expected, at least in an infinite time. More precisely, at the lowest order in thickness variations of a lubrication approximation for the filaments, they narrow exponentially in time. Incoming fingers slow down in the same way, whereas the filaments stretch and the droplets at their tips are centrifuged away also exponentially.

In the high viscosity contrast limit,  $A \rightarrow 1$ , all these exponential behaviors have the same time constant,  $1/t^*$ , where  $t^*$  is the characteristic time scale of the problem, and we have been able to observe all of them and confirm this value by phase-field simulations and experiments. For low viscosity contrasts, the filament thinning has a time constant of  $K = 2/[(1+A)t^*]$  in absolute value, whereas the droplet dynamics remain close to  $K' = 1/t^*$  as for high viscosity contrasts. The droplet scaling is



thus universal in a first approximation, i.e., only weakly dependent on any dimensionless control parameter. Furthermore, we have found it not to be much affected by whether the droplet is isolated or connected to a filament. We have derived an exact time-dependent solution (previously found in the  $A \rightarrow 1$  limit [24]) for the case of an off-center isolated circular droplet which shows that this universality is rigorous for isolated circular droplets.

In a second approximation, droplets at the tip of the filaments are actually found to scale with a time constant slightly below the theoretical value  $1/t^*$ , so that this is always below that of the filament thinning  $2/[(1+A)t^*]$ . Some fraction of the fluid expelled by the filament as it narrows is hence fed into the droplet. Because the time constant for the thinning increases above  $1/t^*$  as  $A$  is decreased, the lower  $A$  the more flux the droplets receive, as observed in both experiments and simulations.

For experiments with two liquids (low  $A$ ), comparison with the exact solution for an isolated circular droplet and extensive simulations have shown the time scale of the dynamics  $t^*$  to be lower than its characteristic value  $t^* = 12(\mu_{\text{in}} + \mu_{\text{out}})/(b^2\Omega^2\Delta\rho)$ . We explain this by an effective lower viscosity of the inner fluid  $\mu_{\text{in}}$ , which comes from Darcy's law corrected to take into account the presence of a wetting layer of the outer liquid. This results in an increased inner liquid mobility.

Although rotation causes infinite-time pinch-off at the lowest order in the variations of the filament thickness, both the thickness decay and the stretching apart of neighboring points smooth out thickness variations. Rotation also enters the other next order term: a non-local term proportional to  $1 - A$ . Because this term is non-local and the interface is necessarily highly curved in the droplets at the end of the filaments, it can overcome the stabilizing effect of the lowest-order contribution of rota-

tion, and thus initiate finite-time pinch-off. The role of surface tension and the interplay with the local and non-local terms associated with rotation remain interesting open questions.

In any case, this non-local term can account for the differences observed in both experiments and simulations, where finite-time pinch-off singularities appear systematically for low values of  $A$  but not for high values of  $A$ . Three-dimensional effects like wetting do not seem to account for the initiation of pinch-off, since simulations are free of them and nevertheless reproduce well the experimental morphologies and the pinch-off phenomenon itself. Corrections due to the non-local term are also the main reason for obtaining a less clear exponential behavior for low viscosity contrasts.

Note that, for the case of a channel under gravity or pressure-driven injection, this non-local term still arises, although it has another form. Therefore, it may also explain the enhancement of finite-time pinch-off observed for low  $A$  in these well known cases.

## VIII. ACKNOWLEDGMENTS

R. F. acknowledges financial support through a European Community Marie Curie fellowship. R. F. and J. C. also thank the Benasque Science Center for hospitality and the European Union high-level scientific conference and the NATO Advanced Studies Institute programs for support during a summer school at which part of this work was carried out. Financial support from Ministerio de Ciencia y Tecnologia (Spain) under project BQU2003-05042-C02-02 and from European Commission's Research Training Network HPRN-CT-2002-00312 (PHYNECS) are acknowledged.

- 
- [1] J. Keller and M. J. Miksis, *SIAM J. Appl. Math.* **43**, 268 (1983).
  - [2] J. Eggers, *Rev. Mod. Phys.* **69**, 865 (1997).
  - [3] M. Moseler and U. Landman, *Science* **289**, 1165 (2000).
  - [4] J. Eggers, *Phys. Rev. Lett.* **89**, 084502 (2002).
  - [5] A. Oron, S. H. Davis, and S. G. Bankoff, *Rev. Mod. Phys.* **69**, 931 (1997).
  - [6] W. W. Zhang and J. R. Lister, *Phys. Fluids* **11**, 2454 (1999).
  - [7] For a way to model scales below the cell gap, see H-G. Lee, J.S. Lowengrub, and J. Goodman, *Phys. Fluids* **14**, 2492 (2002), *Phys. Fluids* **14**, 514 (2002).
  - [8] R.E. Goldstein, A.I. Pesci, and M.J. Shelley, *Phys. Rev. Lett.* **70**, 3043 (1993).
  - [9] T.F. Dupont, R.E. Goldstein, L.P. Kadanoff, and S-M. Zhou, *Phys. Rev. E* **47**, 4182 (1993).
  - [10] R. Almgren, *Phys. Fluids* **8**, 2 344 (1995).
  - [11] R. Almgren, A. Bertozzi, and M. Brenner *Phys. Fluids* **8**, 6 1356 (1996).
  - [12] P. Constantin, T.F. Dupont, R.E. Goldstein, L.P. Kadanoff, M.J. Shelley, and S-M. Zhou, *Phys. Rev. E* **47**, 4169 (1993).
  - [13] R.E. Goldstein, A.I. Pesci, and M.J. Shelley, *Phys. Rev. Lett.* **75**, 3665 (1995).
  - [14] R.E. Goldstein, A.I. Pesci, and M.J. Shelley, *Phys. Fluids* **10**, 2701 (1998).
  - [15] A. Sierou and J. R. Lister, *J. Fluid Mech.* **497**, 381 (2003).
  - [16] P.G. Saffman and G.I. Taylor, *Proc. R. Soc. London A*, **245**, 312 (1958).
  - [17] J. V. Maher, *Phys. Rev. Lett.*, **54**, 1498 (1985).
  - [18] We recall here that injection and gravity are completely equivalent, since both can be reparametrized into a unique driving force.
  - [19] E. Alvarez-Lacalle, J. Casademunt, and J. Ortín, *Phys. Fluids*. **16** 908 (2004).
  - [20] E. Alvarez-Lacalle, J. Casademunt, and J. Ortín, (preprint).
  - [21] As demonstrated in [20], a thin uniform layer of the oil wetting the glass plates is necessary to reproduce the numerical results obtained with standard boundary conditions. This is done in practice by generating an advancing

- stable annulus of the same oil before the experiment is performed (see [33]).
- [22] E. Pauné, *Interface dynamics in two-dimensional viscous flows* Ph. D. thesis, Universitat de Barcelona (2002).
- [23] Z. Csahók, C. Misbah and A. Valance, *Physica D* **128**, 87 (1999).
- [24] F.X. Magdaleno, Ph. D. thesis, Universitat de Barcelona (2000).
- [25] E. Alvarez-Lacalle, J. Casademunt, and J. Ortín, *Phys. Rev. Lett.* **92**, 054501 (2004).
- [26] G. Tryggvason and H. Aref, *J. Fluid Mech.* **154**, 287 (1985).
- [27] For a step-by-step derivation (including a kind of viscosity anisotropy), see R. Folch, J. Casademunt and A. Hernández-Machado, *Phys. Rev. E* **61**, 6632 (2000).
- [28] R. Folch, J. Casademunt, A. Hernández-Machado and L. Ramírez-Piscina, *Phys. Rev. E* **60**, 1724 (1999).
- [29] R. Folch, J. Casademunt, A. Hernández-Machado and L. Ramírez-Piscina, *Phys. Rev. E* **60**, 1734 (1999).
- [30] T. Biben, C. Misbah, A. Leyrat and C. Verdier, *Europhys. Lett.* **63**, 623 (2003).
- [31] C.W. Park and G.M. Homsy, *J. Fluid Mech.* **139**, 291 (1984).
- [32] E. Alvarez-Lacalle, J. Casademunt, and J. Ortín, *Phys. Rev. E* **64**, 016302 (2001).
- [33] L. Carrillo, J. Soriano, and J. Ortín. *Phys. Fluids*. **11** 778 (1999).